Surrogate modelling-assisted comparison of reactor schemes for carbon dioxide removal by enhanced weathering of minerals using seawater

Jinyuan Zhang [a], Aidong Yang [a,*], Richard Darton [a], Lei Xing [b], Adam Vaughan [a]

[a] *Department of Engineering Science, University of Oxford, OX1 3PJ Oxford, UK*
[b] *Department of Chemical Process Engineering, University of Surrey, GU2 7XH Guildford, UK*
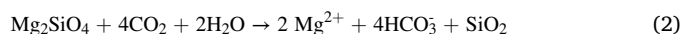
ARTICLE INFO

ABSTRACT

Reactor-based enhanced weathering of minerals represents one of the options for CO_2 removal from the atmosphere to control the concentration of greenhouse gases for stabilising the climate. Earlier studies have modelled two reactor types, namely trickle-bed reactor and packed bubble column. However, their CO_2 removal potential has not been compared. Building on the previous studies, this work further develops the mechanistic reactor models to enable them to consistently describe continuous weathering of minerals using seawater. Addressing the computational demands of the mechanistic models, a surrogate modelling-based optimisation procedure is developed to allow each reactor type to be rigorously optimised for minimising two competing objectives, namely energy consumption and space requirement. This has allowed the Pareto fronts of the two reactor types to be produced and compared. When applied to calcite weathering which is predominantly controlled by gas–liquid mass transfer, the packed-bubble column has been shown to consistently outperform the trickle-bed reactor, thanks to its superior mass transfer performance. However, when considering the weathering of forsterite, packed-bubble column performance is significantly worsened compared to calcite weathering, primarily because its low dissolution rate shifts the controlling mechanism of the process from gas/liquid mass transfer to solid dissolution. These results provide new insights to inform the future evaluation of reactor-based enhanced weathering schemes in terms of reactor design selection and the implication of mineral types.

1. Introduction

As the threat of climate change intensifies, carbon dioxide (CO_2) removal from the atmosphere (CDR) has become a widely recognised option, together with emission reduction, to keep the concentration of greenhouse gases in the atmosphere under control. A significant CDR requirement, in the range of 100–1000 Gt CO_2 by 2100, is considered necessary by the IPCC [1] to meet the 1.5 °C target for limiting the extent of global warming.

Among the approaches that have been suggested for CDR is enhanced weathering (EW) of carbonate or silicate minerals, deployed either in an open environment by spreading mineral particles e.g. on agricultural lands [2] or using engineered reactors [3,4]. This process removes CO_2 through accelerating the weathering reactions between minerals, CO_2 and water, as shown in the following reactions, where calcite and forsterite represent typical carbonate and silicate minerals, respectively:

$$CaCO_3 + CO_2 + H_2O \rightarrow Ca^{2+} + 2HCO_3^- \tag{1}$$

$$Mg_2SiO_4 + 4CO_2 + 2H_2O \rightarrow 2\ Mg^{2+} + 4HCO_3^- + SiO_2 \tag{2}$$

The reaction products, and the bicarbonate ions in particular which carry the removed CO_2, are expected to eventually reach and be stored in the oceans [5]. Recent studies have developed mathematical models to evaluate the reactor-based approach [3,4], following early explorations of mineral weathering in engineered devices [6]. Such reactors offer an enclosed space and controlled conditions to enhance weathering rates, compared to implementation in open environments. However initial modelling results predicted significant energy and water demand, suggesting the need to optimise selection and design of reactor schemes as important steps for further assessing their potential.

Building on previous work on the mathematical modelling of calcite weathering using two reactor types, namely trickle-bed reactor (TBR) [3] and packed bubble column (PBC) [4], this study further develops these models and compares their predicted optimal performance. In terms of reactor modelling, this work extends the earlier studies by (1) depicting continuous solid feeding (as opposed to dosing the solid particles only at the beginning), and (2) converting the previous TBR model to handle weathering with seawater rather than fresh water. These changes, which make the models directly comparable with each other, also improve their applicability to large-scale operations. Earlier work revealed the strong trade-off between energy consumption and carbon removal rate; the latter determines the land area requirement of a reactor scheme: the lower the removal rate, the higher the land area requirement [4]. The optimisation of the two reactors in this work considers the minimisation of two objective functions, namely energy consumption and land area requirement. This is carried out with the assistance of surrogate modelling [7] to avoid prohibitive computational costs of running optimisation directly using the original (mechanistic) reactor models. Following the optimisation, the more promising reactor scheme is further applied to the weathering of forsterite as a representative silicate mineral, to offer a comparison with calcite as a carbonate. These studies contribute to the choice and optimisation of reactor-based EW implementations and to the understanding of the impact of mineral types in such schemes.

2. Methods

2.1. Reactor-based enhanced weathering scheme and two reactor types

A reactor-based scheme for EW of minerals to remove CO_2 from air (Fig. 1), as proposed earlier [4], contains a weathering reactor in which mineral particles are in contact with water and CO_2-containing gas. It has been shown that enriching the gas feed in CO_2 is desirable for accelerating the weathering process [3,4] in the reactor, and both the ambient air feed, and the recycled gas are enriched, as shown in Fig. 1.

The two reactor types considered here are TBR and PBC, both containing a fixed bed of mineral particles but differing in terms of the gas–liquid-solid contacting. In a TBR, liquid travels through the bed downwards in discrete rivulets and droplets which typically wet the particles only partially, while gas rises upwards as a continuous phase. The weathering reaction occurs at the wetted particle surfaces, a portion of which is available for gas–liquid mass transfer [3]. In a PBC, the liquid is the continuous phase while gas travels through the reactor in the form of discrete bubbles. Since the particles in the PBC are submerged in liquid, their surfaces are considered to be fully available for weathering. In the PBC, gas–liquid mass transfer occurs at the surface of the gas bubbles [4].

The CO_2 enrichment devices considered in the scheme assessed here
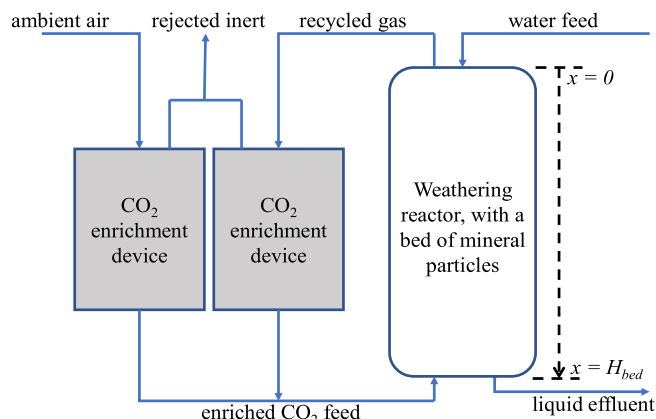

Fig. 1. Reactor-based EW scheme (adapted from [4]).

are yet to be fully developed, though they are of the type currently being considered for Direct Air Capture (DAC) of CO_2. Such processes, currently aiming to produce pure CO_2 [8] from ambient air, could supply streams with lower CO_2 enrichment (say 1–10 % CO_2) at a lower energy cost [9]. Using the same treatment as in previous work [4], this study focuses on the modelling of the reactors and adopts a theoretical estimation for the energy consumption of CO_2 enrichment.

2.2. Mechanistic reactor modelling

Although previous work has developed mathematical models for EW using TBR and PBC, comparison between the two reactor types was difficult because the TBR used freshwater [3] and the PBC used seawater [4]. Given the large water consumption of the weathering process, the use of seawater is more likely in practice, so the TBR model has been adapted to use seawater. Furthermore, both existing models assumed a batch operation in terms of the loading of the mineral particles. In this work, continuous feeding of solids is modelled, which is a more probable operating strategy. Following these adaptations, both the TBR and the PBC models, still assuming calcite as the mineral for weathering, are then optimised and predicted performances compared. Subsequently, a further model adaptation is made, to incorporate the dissolution kinetics of forsterite. This permits us to compare the performance of the optimised reactor between a model silicate (forsterite) and a model carbonate (calcite). In the rest of this section, the core principles of the two reactor models, implemented in previous work and retained in this study, are first summarised, which is followed by a description of the introduced changes.

2.2.1. Core principles of the reactor models
The one-dimensional dynamic mechanistic model for each reactor is based on mass conservation of the gas, liquid and solid phases. The detailed model equations can be found in previous work in full detail [3,4] and are not repeated here; instead, the core principles are summarised.

2.2.1.1. Mass transfer and gas/liquid hold-ups. The gas–liquid mass transfer of CO_2 in both reactors was modelled using specific mass transfer area (a_{GL}) and overall (liquid phase) mass transfer coefficient (K_{OL}). For the TBR, these were determined by Onda's correlations [10,11], with a_{GL} as a fraction of the specific surface area of the solid particles. The liquid hold-up was estimated according to Billet and Schultes [12,13]. For the PBC, a_{GL} was derived from gas hold-up and bubble size; the former was estimated by the sum of a static and a dynamic component according to experimental analyses [14,15], while the latter was based on a correlation by Akita & Yoshida [16]. The K_{OL} in the PBC model was estimated using Danckwerts' formulation based on surface renewal analysis [17].

2.2.1.2. Reactions. The relatively slow processes, namely the dissolution of calcite and the conversion of dissolved CO_2 in the liquid phase to bicarbonate ions, were modelled by their respective kinetic equations. The change in mineral particle size was related to the dissolution of the particles (assumed spherical) by mass balance. The other aqueous phase reactions were treated through chemical equilibria, complemented by electrical charge balance.

2.2.1.3. Energy consumption. As detailed in the PBC model [4], energy is consumed by the pumping of water to the top of the reactor, compression of gas feed as required to overcome pressure drop through the reactor, preparation (crushing and commutation) of solid particles to the specified size, and CO_2 enrichment. All of these consumptions are considered for both reactors in this work. The energy consumption for supplying gas and liquid feeds follows the treatment adopted previously for the TBR [3] and the PBC [4]. The energy consumption for preparing

solid particles and CO_2 enrichment are as previously suggested in the PBC model [4].

2.2.2. Modelling of a reactor with continuous solid feeding

Both existing TBR and PBC models assume that the reactor is initially filled with the mineral particles, with the bed shrinking as dissolution of the particles progresses. Continuous solid feeding, implemented in this work, means that after the initial placement of the particles, additional particles are introduced to the top of the bed such that the total height of the bed remains constant despite the dissolution process. This leads to a population of particles inside the reactor with differing ages. Unlike the previous simplified models where a single particle size was assumed across the bed throughout the simulation, the adapted models here capture the change of the particle size along the axial dimension during the simulated period due to dissolution and downward movement of particles. Adopting an approach similar to that previously used to model solid biomass changes in an evolving biofilm [18,19], a conservation equation for the particle surface area per unit bed volume, denoted by a_s (m^{-1}), is used:

$$\frac{\partial a_s}{\partial t} + \frac{\partial (v a_s)}{\partial x} = R_a \tag{3}$$

$$a_s|_{x=0} = a_{s0} \tag{4}$$

where t (s) is time, x (m) is the (axial) spatial co-ordinate, v (m s^{-1}) is the advective velocity of the bed due to particle dissolution, and a_{s0} (m^{-1}) is the specific surface area at the (top) feeding layer of the bed, determined by the size of the feed particles and bed porosity (see equations (9) and (10)). R_a (m^{-1} s^{-1}) denotes the rate of reduction of a_s due to dissolution and can be calculated as follows (for derivation, see Supplementary Material, Section S1):

$$R_a = -12(1 - \epsilon) d_p^{-2} \rho_p^{-1} M_p R_d \tag{5}$$

where ϵ is the bed porosity and remains approximately constant (~0.39) for the range of particle size and bed diameter considered in this work, d_p is the particle diameter, M_p (kg mol^{-1}) is the molecular weight of the particles, ρ_p (kg m^{-3}) is the particle density, and R_d (mol m^{-2} s^{-1}) is the specific surface dissolution rate, determined by the dissolution kinetics incorporated in the existing weathering reactor models [3,4].

The advective velocity v is modelled as below:

$$\frac{\partial v}{\partial x} = -\frac{R_m}{\rho_p} \tag{6}$$

$$v|_{x=H_{bed}} = 0 \tag{7}$$

where R_m (kg m^{-3} s^{-1}) is the mass rate of particle dissolution (per unit particle volume) and is calculated from R_d:

$$R_m = R_d a_p M_p \tag{8}$$

a_p (m^{-1}) is the specific surface area per unit volume of particle, related to a_s and particle diameter d_p (m) by:

$$a_s = a_p(1 - \epsilon) \tag{9}$$

$$a_p = 6/d_p \tag{10}$$

2.2.3. Further changes to the TBR model

In addition to adopting a continuous solid feed, the existing TBR model was adapted to use seawater for dissolving calcite particles. The same kinetics equation for calcite dissolution in seawater as in the existing PBC model [4] was used, which had been specifically derived from seawater-based dissolution experimental data as opposed to the one previously used in the TBR model which was originally developed for dissolution in freshwater. An additional important change is that the TBR model now accounts for the out-gassing of dissolved CO_2 from the

liquid effluent of the weathering reactor when it comes into contact with the ambient environment. This is now similar to the PBC model [4], in which an equilibrium calculation deduces the loss of CO_2 captured in the reactor, to determine the net CO_2 removal.

2.2.4. Modelling kinetics of forsterite dissolution

Forsterite dissolution is considered to follow the chemical reaction below:

$$Mg_2SiO_4 + 4H^+ \Leftrightarrow H_4SiO_4 + 2Mg^{2+} \tag{11}$$

The specific surface dissolution rate R_d is modelled by adopting a previously proposed kinetics equation [20] to account for the effect of saturation:

$$R_d = \left[A_1 e^{\frac{-E_1}{RT}} (a_{H^+})^n + A_2 e^{\frac{-E_2}{RT}} \right] \left(1 - \frac{Q}{K_{eq}} \right) \tag{12}$$

where A_1 (A_2) (mol m^{-2} s^{-1}) is the pre-exponential Arrhenius constant and E_1 (E_2) (kJ mol^{-1}) is activation energy to account for the dissolution with (without) the impact of pH. T (K) is temperature, R (kJ mol^{-1} K^{-1}) is the gas constant, a_{H+} (mol L^{-1}) is the activity of hydrogen ions, n is the reaction order for hydrogen ions, Q (L mol^{-1}) is reaction activity coefficient and K_{eq} (L mol^{-1}) is the equilibrium constant of dissolution.

The reaction activity quotient is given by:

$$Q = \frac{a_{H_4SiO_4}(a_{Mg^{2+}})^2}{(a_{H^+})^4} \tag{13}$$

The temperature-dependent equilibrium constant, K_{eq}, is given by the following correlation:

$$log_{10}K_{eq}(T) = A + BT + \frac{C}{T} + Dlog_{10}T + \frac{E}{T^2} \tag{14}$$

where the constants were obtained from the Thermoddem geochemical database [26]. Further details of the calculation of activity coefficients and the parameter values adopted for equations (12) and (14) are provided in Supplementary Material (Section S2).

2.3. Surrogate model-based two-objective optimisation

2.3.1. Formulation of the optimisation problem

Each reactor is optimised by considering the minimisation of two competing objective functions, namely the specific energy consumption, SEC, in GJ tonne^{-1} and the specific space requirement, SAR, in m^2 (tonne yr^{-1})$^{-1}$, where "tonne" refers to CO_2 removal. In this study, every reactor simulation run was for the continuous operation of 1 year starting from a bed filled with particles at their initial size, and the SEC and SAR used in optimisation were average values over the year. A weighted sum method is adopted to combine the two objectives:

$$\text{Minimise } y = w \cdot SEC + (1 - w) \cdot SAR \tag{15}$$

During the computational procedure, the weighting factor w increases from 0 to 1 by an increment (set to be 0.05). At each value of w, the optimisation problem is solved to produce one solution point; all the solution points collectively form the Pareto front curve as the overall result of the two-objective optimisation. The chosen increment in w proved to be able to yield Pareto front curves with adequate shapes (see Figs. 4 and 5).

The independent or decision variables are listed in Table 1. Note that the gas and liquid superficial velocities (u_G, u_L) of the TBR are not directly manipulated. Instead, they are indirectly controlled via the flow parameter (F_{lv}) and the operating parameter (OP), with their upper limits set to 0.4 and 0.5 to retain the operating regime to trickle flow and to avoid flooding, respectively. The relationship between u_G/u_L and F_{lv}/OP at several values of F_{lv} was given in [3], which was used as the basis for interpolation in this work to enable the simulation at arbitrary values of F_{lv} within its specified range. All the other range settings, intended to

Table 1
Decision variables and their ranges.

Decision variables	Unit	Range for TBR	Range for PBC
Reactor feed CO_2 concentration (mol fraction) ($x_{CO_2,0}$)	–	[1e-2, 3e-1]	[1e-2, 3e-1]
Flow parameter (F_{lv})	–	[1e-1, 4e-1]	–
Operating parameter (OP)	–	[1e-1, 5e-1]	–
Superficial gas velocity (u_G)	m s^{-1}	–	[1e-3, 1e-2]
Liquid to gas superficial velocity ratio	–	–	[1e-2, 5e-1]
Solid bed height (H_{bed})	m	[5e–1,20]	[5e–1,20]
Initial particle radius, for calcite (r_{p0})	m	[1e-3, 1e-2]	[1e-3, 1e-2]

ensure the coverage of conditions leading to the optimal trade-off between the two competing objectives, were determined by preliminary simulation tests.

2.3.2. Optimisation procedure

To avoid the computational costs of running an optimisation algorithm directly on the partial differential equations (PDE)-based mechanistic reactor models, a procedure using surrogate models to ease the computational burden was adopted, as shown in Fig. 2.

The procedure begins with obtaining mechanistic simulation results at inputs specified by an initial, "space-filling" sampling design over the space determined by the ranges of the decision variables (Table 1), using Latin Hypercube Sampling (LHS) [21]. This generates the dataset for building the initial surrogate model for each of the two objectives (step 2), with each datum comprising inputs (i.e. decision variables) and the corresponding reactor optimisation objective. To choose the most suitable machine learning model, a number of options were tested and compared, including artificial neutral network (ANN) [22], radical basis function, Gaussian process regressor, linear regression, random forest regression, support vector machine, gradient boosting regressor,

Initial sampling design

1. Initiating or updating training dataset by simulations using mechanistic model

2. Training surrogate model

3. Initiating ($w = 0$) or increasing weight (w); multi-objective optimisation using surrogate model

4. Validation of surrogate model on optimal solution

5. Generating additional sampling design

Error criterion met? — No

Yes

All values of w calculated? — No

Yes

6. Premature convergence checking and correcting

Pareto front established

Fig. 2. Procedure for surrogate model-based two-objective optimisation.

extreme gradient boosting regressor etc. ANN was eventually chosen for its best performance in terms of generalization accuracy, based on the mean square error on the test set. The determination of hyperparameters of each ANN mode was guided by parameter sweep. Subsequently, the two ANN models, each predicting one of the two objectives, are used to compute the weighted sum of the two objectives (Equation (15)), replacing the mechanistic reactor model, in optimization with a specific value of w (step 3) which adopts the Genetic Algorithm as an effective derivative-free method [23]. Each run of this step produces a solution point (corresponding to the current value of w), at which the accuracy of the surrogate model is evaluated against the mechanistic model (step 4). Tested against a relative effort threshold of 5 %, an inaccurate surrogate model is re-trained (step 2) with an augmented dataset including additional samples in the vicinity of the solution point generated by further mechanistic simulation runs (steps 5 and 1); this procedure (steps 1–5) is repeated until a solution point is obtained from surrogate models with satisfactory accuracy. In this work, a sample size of ∼ 400 data points for the initial training and 30 for additional sampling were found adequate.

Finally, after the optimization runs at all values of w have been conducted, the computed solution points are examined against the expected trend that a solution point from an increased value of w should correspond to a SEC no lower than that before the increase in w (cf. Equation (15)). A violation of this trend indicates premature convergence of the computation of the solution point in question; this solution point is then re-computed with the surrogate model re-trained using the latest (and enlarged) data set until the expected trend is obtained (step 6).

2.4. Implementation of simulation and optimisation

All mechanistic reactor models were implemented in multi-physics modelling software COMSOL Multiphysics (version 5.5). The surrogate model-based optimisation was implemented in Python. The link between python and COMSOL Multiphysics was established using a Python scripting interface for COMSOL Multiphysics MPh 1.1.5 [24].

3. Results and discussion

### 3.1. Execution of the optimization procedure

The surrogate model-based optimisation procedure was successfully applied to the TBR and the PBC for calcite weathering. The chosen surrogate model type, i.e. ANN, was proven to offer good prediction accuracy, as demonstrated in Fig. 3 for the models built from the initial dataset, where the RMSE (root-mean-square error) and R^2 were both calculated on testing data.

As shown in Fig. 4, for each reactor, the whole optimisation procedure was able to effectively guide the additional sampling (i.e. mechanistic simulation runs) to move from the initial (space-filling) samples to those located in the vicinity of what was eventually established as the optimal solution points (i.e. the Pareto front).

3.2. Reactor performance comparison

The Pareto fronts for the two calcite weathering reactors are compared in Fig. 5, which shows that the PBC clearly outperforms the TBR across all the trade-off positions between SEC and SAR. The PBC model, as the model for a more promising reactor type than TBR, has therefore been adapted to forsterite weathering, and the surrogate model-based optimisation procedure subsequently applied to the PBC-forsterite model (with the same decision variable ranges as shown for PBC in Table 1, except for the particle size, see Section 3.2.2). As shown by its resulting Pareto front, also displayed in Fig. 5, the forsterite case incurs considerably greater energy consumption or area requirement than the calcite case.
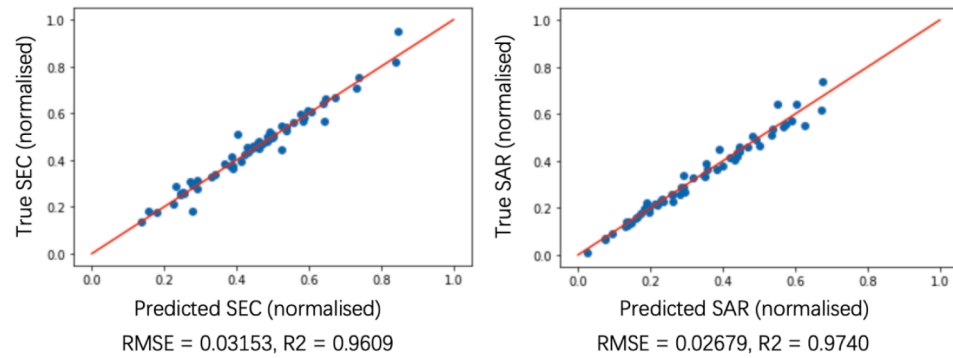
To gain further insights regarding the comparisons, Table 2 shows
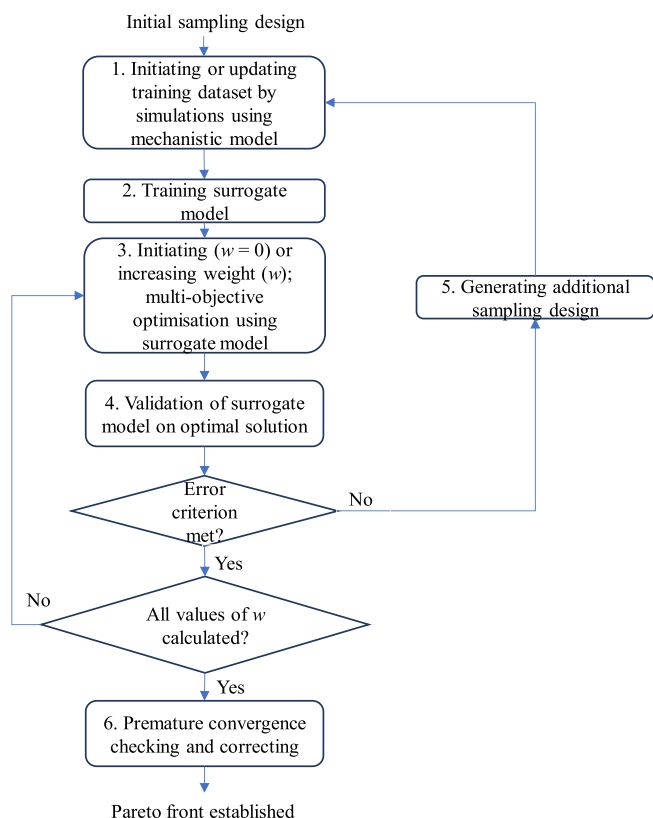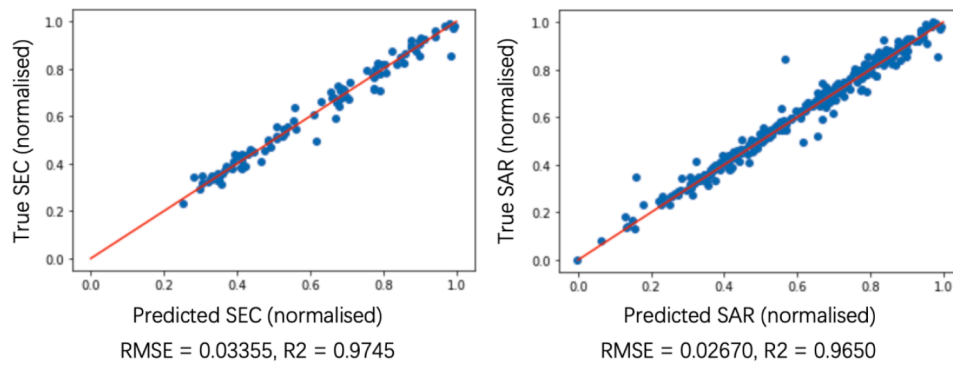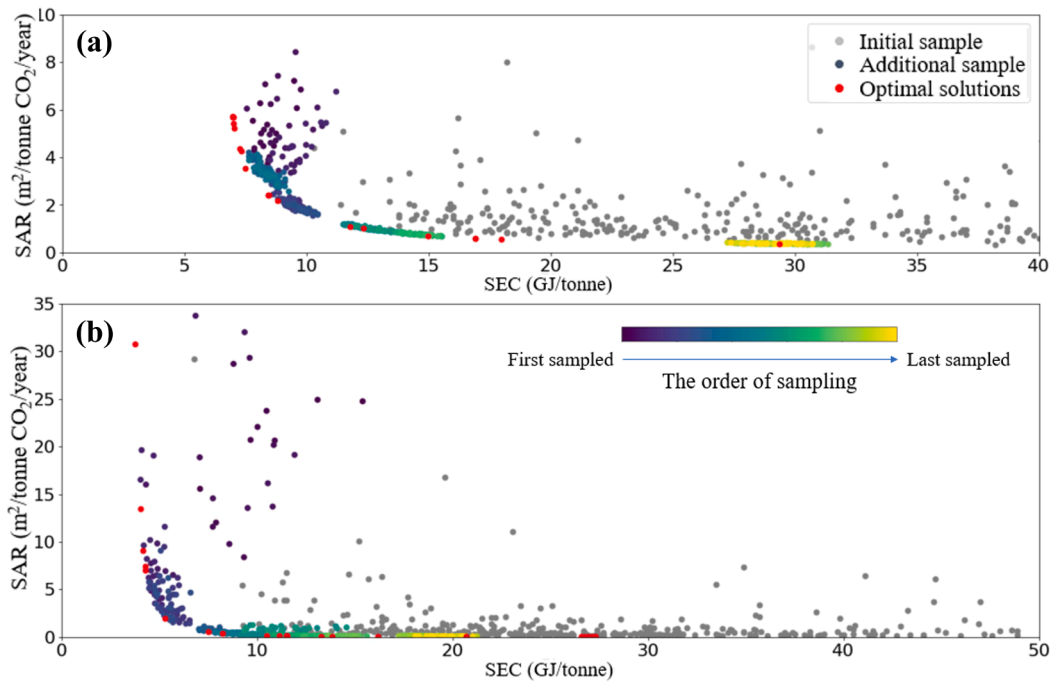
(a) TBR-calcite

(b) PBC-calcite

Fig. 3. Accuracy of the initial surrogate models in terms of RMSE and R^2. Left: the *SEC* model; Right: the SAR model.

Fig. 4. Additions of new samples in the course of optimization for (a) TBR-calcite reactor and (b) PBC-calcite reactor. The "order of sampling" depicted by variation in colour in both (a) and (b) refers to the introduction order of the samples during the optimization procedure.
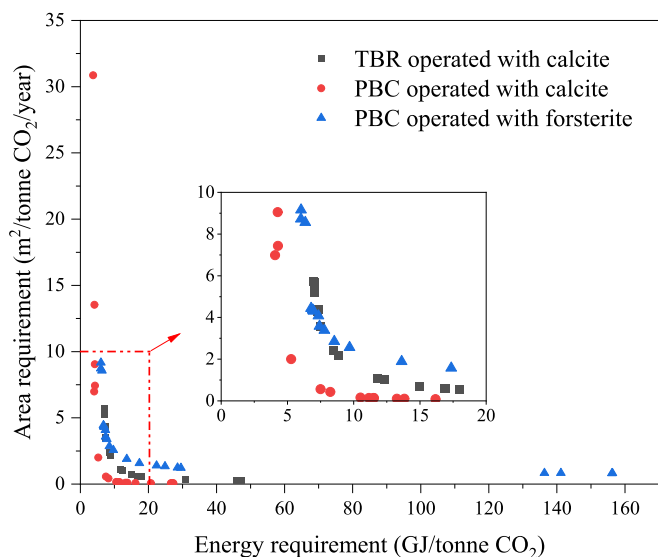
Fig. 5. Overall pareto fronts from three optimisation runs.

the *SEC* and the SAR for three positions of the Pareto front of each reactor case (TBR with calcite, PBC with calcite, and PBC with forsterite, referred to as TBR-C, PBC-C and PBC-F, respectively) shown in the inset of Fig. 2: "low energy", "trade-off", and "low area", corresponding respectively to the upper left point, the lower left corner, and the lower right point.

3.2.1. Comparison between TBR and PBC

As shown in the previous modelling studies [3,4], the CO_2 removal through calcite weathering in both reactors is primarily controlled by gas–liquid mass transfer of CO_2, although in the high-rate region the role of dissolution kinetics tends to become more visible. Table 2 shows that the same increasing trends in the optimal u_G, u_L, H_{bed} and $x_{CO2,o}$ are shared by the two reactors, when the reactor setting moves from a low-energy region to a low-area (i.e. high removal rate) region. However, their mass transfer performance is rather different, with the PBC being generally better than the TBR, as shown in Fig. 6 (specific gas–liquid mass transfer area, a_{GL}) and Fig. 7 (volumetric mass transfer coefficient, $K_{OL}*a_{GL}$). In particular, the volumetric mass transfer coefficient of PBC is approximately double that of TBR at their respective optimal trade-off settings. This contributes to a nearly 40 % reduction in *SEC* (from 8.45 to 5.29 GJ tonne^{-1}) together with the lowering of SAR (~17 %, from 2.41 to 2 m^2 (tonne yr^{-1})$^{-1}$). Compared to the TBR, the optimal trade-off setting of the PBC involves significantly lower H_{bed} (1.05 vs 9.39 m) and u_G (9.82 × 10^{-4} vs 2.13 × 10^{-2} m s^{-1}), both contributing to energy consumption reduction, while u_L and $x_{CO2,o}$ are more comparable between the two reactors.

In terms of the optimal particle size, the PBC preferred the lower bound of the considered range; it offers the maximum specific surface area for mineral dissolution, although the impact on the overall performance is modest because of the significant dominance of gas/liquid mass transfer. It should be noted that the particle size also affects mass transfer in the PBC through influencing the static gas holdup, although its impact is insignificant within the considered range of particle size [4]. For the TBR, there is a more direct link between particle size and gas–liquid mass transfer area: the latter is the fraction of the total particle surface that is "wetted"; this fraction is significantly influenced by the gas and liquid velocities and has been shown to be rather small for the considered range of reactor settings [3]. The optimisation results show that to pursue lower reactor area requirements (through higher CO_2 removal rates), the chosen TBR settings (in particular, with increasing u_G and u_L) led to a desirable increase in a_{GL} (Fig. 6), despite larger particle sizes (corresponding to lower total particle surface areas) being chosen (Table 2) probably to curb the increase in pressure drop (hence energy consumption) in such settings.

Finally, although the surface area available for mineral dissolution is not of great significance for calcite weathering, it is worth noting that in the PBC, the particles are submerged in a continuous liquid phase so that their surface area is fully available for dissolution. In contrast, the dissolution of minerals in the TBR occurs only at the wetted particle surface due to the discrete nature of the trickle flow, which can be a very small fraction of the solid surface, as shown in Fig. 8. This limitation will become much more important for dissolution-controlled weathering, such as the case of forsterite.

3.2.2. Comparison between calcite and forsterite weathering in PBC

Compared to calcite, the weathering of forsterite in the PBC (i.e. the more promising reactor type) was predicted to be more challenging: At the optimal trade-off setting, it requires ~ 60 % more *SEC* (8.54 GJ
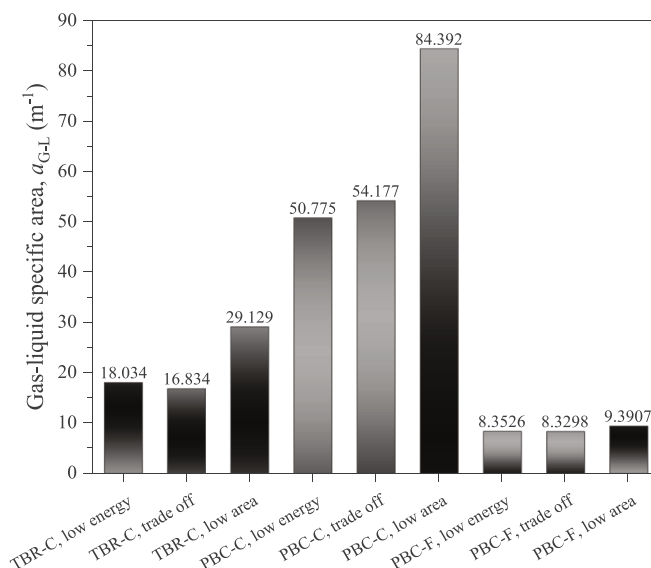

Fig. 6. Calculated gas–liquid specific areas in different cases.

Table 2
Optimal reactor settings and performance.

	SEC (GJ tonne^{-1})	SAR (m^2 (tonne yr^{-1})$^{-1}$)	u_G (m s^{-1})	u_L (m s^{-1})	H_{bed} (m)	*xinlet CO2* (%)	r_p (mm)
TBR-C, low energy	6.97	5.71	1.85 × 10^{-2}	1.85 × 10^{-4}	4.09	2.26	1.40
TBR-C, trade off	8.45	2.41	2.13 × 10^{-2}	2.70 × 10^{-4}	9.39	4.28	1.92
TBR-C, low area	18.0	0.547	6.96 × 10^{-2}	8.80 × 10^{-4}	20.0	13.1	3.06
PBC-C, low energy	4.27	9.05	4.01 × 10^{-4}	1.34 × 10^{-4}	0.539	1.67	1.01
PBC-C, trade off	5.29	2.00	9.82 × 10^{-4}	3.65 × 10^{-4}	1.05	3.32	1.01
PBC-C, low area	16.2	0.08	9.85 × 10^{-3}	4.44 × 10^{-3}	8.94	15.1	1.01
PBC-F, low energy	6.02	8.72	1.01 × 10^{-4}	1.33 × 10^{-5}	9.43	4.28	5.00 × 10^{-2}
PBC-F, trade off	8.54	2.85	1.28 × 10^{-4}	1.98 × 10^{-5}	20.0	16.4	5.00 × 10^{-2}
PBC-F, low area	17.4	1.57	3.35 × 10^{-4}	6.90 × 10^{-5}	20.0	27.8	5.00 × 10^{-2}

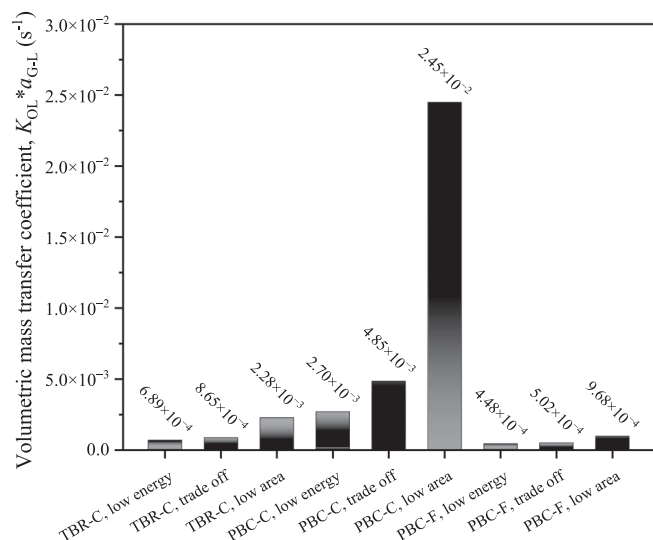**Fig. 7.** Calculated overall mass transfer coefficient in different cases.

calcite, to offer greater mineral dissolution surfaces (by hosting more particles) and to enhance mineral dissolution rate by a lower pH in the liquid phase (through greater dissolution of CO_2 in water), respectively, both of which enhance mineral dissolution in the reactor.

3.3. Other considerations

As described in Section 2.2, this work has introduced a number of changes to the previously developed TBR and PBC models to make them more suitable for a consistent comparison of continuously operated weathering reactors with seawater. Nevertheless, some of the limitations of the previous models were still inherited. Most notably, the energy consumption estimation for CO_2 enrichment still employs a theoretical approximation, as detailed knowledge of practical devices for this purpose is still very limited [4]. For the same reason, the calculated area requirement includes the weathering reactor and omits the (presumably much smaller) space requirement of the CO_2 enriching device. On energy consumption, Fig. 9 shows that CO_2 enrichment occupies a significant proportion of the total consumption. However, its shares are similar between TBR and PBC, so this is unlikely to affect the comparison between the two reactor types much. It can also be seen from Fig. 9 that the share of mineral preparation (including grinding, see [4]) in a reactor-based engineered EW scheme is relatively insignificant, which is a noticeable difference from EW schemes implemented in the open environment (e.g. spreading crushed rocks on farming land) where the supply of suitable minerals represents a major energy demand [2]. Between the two calcite weathering reactors, energy consumption by liquid pumping in TBR-C represents a greater fraction, mainly due to the greater reactor height chosen by the optimisation; its gas pumping fraction did not show the same trend, thanks to its relatively modest pressure drop (per unit reactor height). Between the two PBC reactors, the fraction of energy consumption by gas pumping is greater in PBC-F than in PBC-C, particularly with the low-energy case. This is caused by PBC-F having a reactor height ~ 20 times greater than those of PBC-C, while the former's gas velocity is only ~ 4 times lower than the latter. The difference in liquid pumping between the two reactors is less significant, because the burden of the reactor height of PBC-F is more significantly offset by the reduction in its liquid velocity (~10 times

tonne^{-1}, compared to 5.29 GJ tonne^{-1}) while the SAR increases also by ~ 40 % (2.85 m^2 (tonne yr^{-1})$^{-1}$, compared to 2.00 m^2 (tonne yr^{-1})$^{-1}$). These disappointing results reflect the low specific surface dissolution rate of forsterite, which remains about two orders of magnitude lower than that of calcite, at the reactor conditions simulated in this work. A much smaller forsterite particle size (0.1 mm diameter) was adopted to increase particle surface area (Fig. 8) and thus offer some compensation to its slow dissolution kinetics. This smaller particle size adversely affects the gas–liquid mass transfer (Fig. 7) primarily due to a decrease in the mass transfer area (caused by the reduction in static gas hold up), although this is a rather minor impact compared to the unfavourable dissolution kinetics.

Among the other optimised settings, the optimal u_G and u_L chosen for the forsterite case are much lower than those for calcite weathering, since higher values would not affect the slow kinetics bottleneck. In contrast, the optimal H_{bed} and $x_{CO2,0}$ are both higher than those for
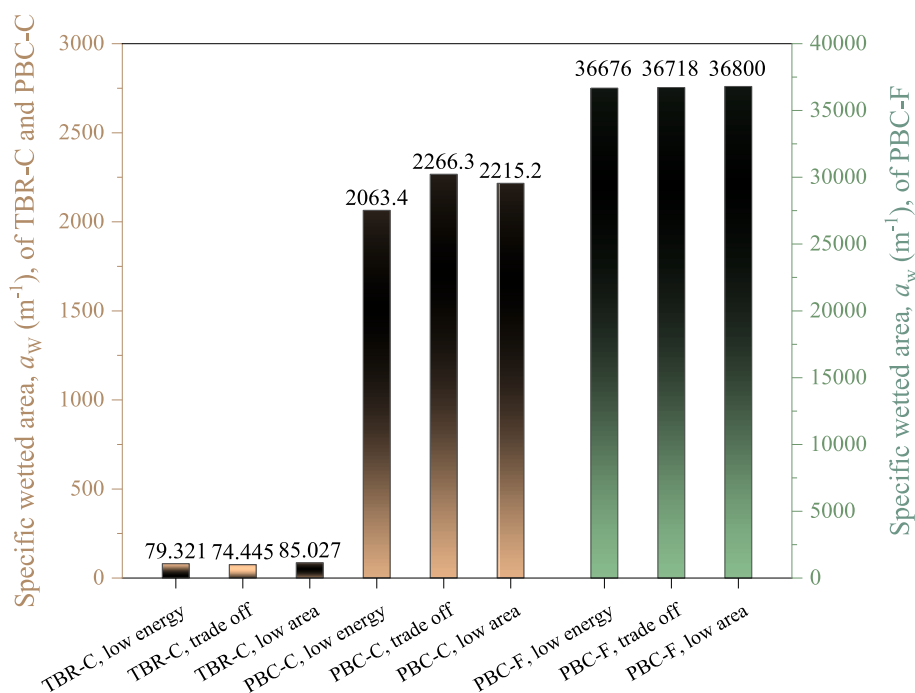

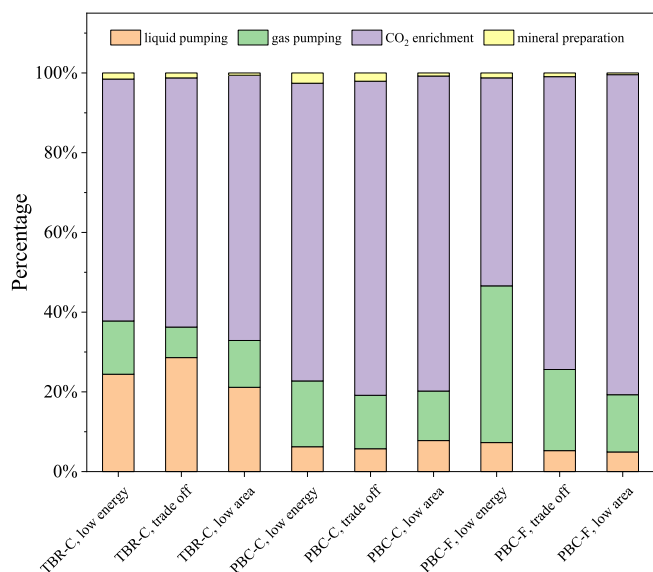**Fig. 8.** Calculated specific wetted area in different cases.

Fig. 9. Shares of energy consumption by different demands for operating EW reactors.

lower than that of PBC-C).

In the case of forsterite weathering, we have shown that the slow dissolution kinetics significantly restricts its performance. While adopting a smaller particle size provides some compensation through increasing the supply of particle surface area, too small particles would make the operation of a PBC (which features a fixed solid bed) infeasible. One alternative is a 3-phase slurry reactor which in principle has the capacity of accommodating very fine particles. However, for a given reactor volume, the acceptable upper limit of the solid fraction in the slurry, dictated by the agitation energy cost and operational practicality [25], requires a detailed assessment of the trade-off between the reduced amount of solid particles and the enlarged (specific) particle surface area.

Finally, our previous work incorporated experimental validation of the earlier version PBC-C model before the feature of continuous solid feeding was introduced. The present modelling work has not involved further experimental validation, although the main modelling elements newly introduced in this study were all based on established literature. As mentioned earlier, the modelling of continuous solid feeding was based on an approach originally developed for modelling biofilms (see Section 2.2.2). The weathering with seawater, now adopted by the TBR model and involving seawater-specific calcite weathering kinetics and parameters for chemical reaction equilibria, was previously established (with experimental validation) in PBC modelling (Section 2.2.3). The kinetics of forsterite weathering, needed for the PBC-F model, was based on a well-known source (Section 2.2.4). Nevertheless, direct experimental studies of these reactor types would be desirable to further assess the reliability of the results.

4. Conclusions

This work has introduced important changes to the existing mathematical models of two weathering reactor types, TBR and PBC, to enable both models to represent consistently the weathering of continuously fed mineral particles in seawater. Combined with the development and application of a robust computational procedure for surrogate model-based multi-objective optimisation, these two reactor types have been rigorously compared considering different trade-off positions of two competing objectives, energy consumption and space (area) requirement. With the weathering of calcite, the PBC has been clearly shown to be more efficient than the TBR, thanks to its better mass transfer

performance, with the optimal trade-off solution predicting an energy consumption of 5.29 GJ tonne^{-1} CO_2 at a modest space requirement. However, a ~ 60 % rise in the optimal trade-off energy consumption has been predicted for PBC-based weathering of forsterite, accompanied by ~ 40 % increase to the corresponding area requirement. This is due to the much slower dissolution kinetics of forsterite compared to that of calcite, which shifts the predominant control mechanism in the process from gas-liquid mass transfer to mineral dissolution which considerably reduces the rate of CO_2 removal. Overall, this work has clearly identified the advantage of the PBC over the TBR in mass transfer, and quantified the challenges associated with the use of slow-dissolving minerals for enhanced weathering. We expect that the modelling approaches and learning from this work will inform future exploration of reactor designs, together with the further investigation of devices for CO_2 enrichment, to reliably establish the true potential of reactor-based enhanced weathering for atmospheric CO_2 removal.

Declaration of Competing Interest

The authors declare that they have no known competing financial interests or personal relationships that could have appeared to influence the work reported in this paper.

Data availability

Data will be made available on request.

Appendix A. Supplementary data

Supplementary data to this article can be found online at https://doi.org/10.1016/j.cej.2023.141804.

References

[1] IPCC. Summary for policymakers. In: Masson-Delmotte V, Zhai P,Pörtner HO, et al., eds. Global Warming of 1.5°C. An IPCC Special Report on the Impacts of Global Warming of 1.5°C Above PreIndustrial Levels and Related Global Greenhouse Gas Emission Pathways, in the Context of Strengthening the Global Response to the Threat of Climate Change, Sustainable Development, and Efforts to Eradicate Poverty. Geneva, Switzerland: World Meteorological Organization; 2018:32.

[2] D.J. Beerling, E.P. Kantzas, M.R. Lomas, P. Wade, R.M. Eufrasio, P. Renforth, B. Sarkar, M.G. Andrews, R.H. James, C.R. Pearce, J.-F. Mercure, H. Pollitt, P. B. Holden, N.R. Edwards, M. Khanna, L. Koh, S. Quegan, N.F. Pidgeon, I. A. Janssens, J. Hansen, S.A. Banwart, Potential for large-scale CO2 removal via enhanced rock weathering with croplands, Nature 583 (7815) (2020) 242–248.

[3] L. Xing, R.C. Darton, A. Yang, Enhanced weathering to capture atmospheric carbon dioxide: modeling of a trickle-bed reactor, AIChE J 67 (5) (2021), https://doi.org/10.1002/aic.17202.

[4] L. Xing, H. Pullin, L. Bullock, P. Renforth, R.C. Darton, and A. Yang, Potential of enhanced weathering of calcite in packed bubble columns with seawater for carbon dioxide removal, Chemical Engineering Journal. 431 (2022) 134096. <doi: 10.1016/j.cej.2021.134096>.

[5] J. Hartmann, A.J. West, P. Renforth, P. Köhler, C.L. De La Rocha, D.A. Wolf-Gladrow, H.H. Dürr, J. Scheffran, Enhanced chemical weathering as a geoengineering strategy to reduce atmospheric carbon dioxide, supply nutrients, and mitigate ocean acidification, Reviews Of Geophysics 51 (2) (2013) 113–149.

[6] G.H. Rau, CO2 mitigation via capture and chemical conversion in seawater, Environ. Sci. Tech. 45 (3) (2010) 1088–1092, https://doi.org/10.1021/es102671x.

[7] A. Bhosekar, M. Ierapetritou, Advances in surrogate based modeling, feasibility analysis, and optimization: a review, Comput. Chem. Eng. 108 (2018) 250–267.

[8] F. Sabatino, A. Grimm, F. Gallucci, M. van Sint Annaland, G.J. Kramer, M. Gazzani, A comparative energy and costs assessment and optimization for direct air capture technologies, Joule 5 (8) (2021) 2047–2076.

[9] R.C. Darton, A. Yang, Removing carbon dioxide from the air to stabilise the climate, in: S.K. Sidkar, F. Priciotta (Eds.), Advances in Carbon Management Technologies, CRC Press, Boca Raton, 2020, pp. 3–22.

[10] K. Onda, H. Takeuchi, Y. Okumoto, Mass transfer coefficients between gas and liquid phases in packed columns", J. Chem. Eng. Jpn. 1 (1) (1968) 56–62, https://doi.org/10.1252/jcej.1.56.

[11] B.I. Dvorak, D.F. Lawler, J.R. Fair, N.E. Handler, Evaluation of the onda correlations for mass transfer with large random packings, Environ. Sci. Tech. 30 (1996) 945–953, https://doi.org/10.1021/es950408+.

[12] R. Billet, M. Schultes, Fluid dynamics and mass transfer in the total capacity range of packed columns up to the flood point, Chem. Eng. Technol. 18 (6) (1995) 371–379, https://doi.org/10.1002/ceat.270180602.

[13] R. Billet, M. Schultes, Prediction of mass transfer columns with dumped and arranged packings, Chemical Engineering Research And Design. 77 (6) (1999) 498–504, https://doi.org/10.1205/026387699526520.

[14] J.G.G. Maldonado, D. Bastoul, S. Baig, M. Roustan, G. Hébrard, Effect of solid characteristics on hydrodynamic and mass transfer in a fixed bed reactor operating in co-current gas–liquid up flow, Chemical Engineering And Processing: Process Intensification. 47 (2008) 1190–1200, https://doi.org/10.1016/j.cep.2007.02.013.

[15] J.H.P. Collins, A.J. Sederman, L.F. Gladden, M. Afeworki, J. Douglas Kushnerick, H. Thomann, Characterising gas behaviour during gas–liquid co-current up-flow in packed beds using magnetic resonance imaging, Chem. Eng. Sci. 157 (2017) 2–14, https://doi.org/10.1016/j.ces.2016.04.004.

[16] K. Akita, F. Yoshida, Gas Holdup and Volumetric Mass Transfer Coefficient in Bubble Columns. Effects of Liquid Properties, Ind. Eng. Chem. Proc. Des. Dev. 12 (1) (1973) 76–80.

[17] P. V. Danckwerts, Significance of liquid-film coefficients in gas absorption, industrial & engineering chemistry. 43.6 (1951) 1460-1467. doi: 10.1021/ie50498a055.

[18] O. Wanner, W. Gujer, A multispecies biofilm model, Biotechnology And Bioengineering. 28 (3) (1986) 314–328, https://doi.org/10.1002/bit.260280304.

[19] Z. Yang, A. Yang, Modelling the impact of operating mode and electron transfer mechanism in microbial fuel cells with two-species anodic biofilm, Biochem. Eng. J. 158 (2020), 107560, https://doi.org/10.1016/j.bej.2020.107560.

[20] J.L. Palandri and Y.K. Kharaka, A compilation of rate parameters of water-mineral interaction kinetics for application to geochemical modeling. U.S. Geological Survey Pen File Report (2004) 1068.

[21] W.L. Loh, On latin hypercube sampling, The Annals Of, Statistics 24 (5) (1996), https://doi.org/10.1214/aos/1069362310.

[22] P. Arabshahi, Fundamentals of artificial neural networks [Book Reviews], IEEE Trans. Neural Netw. 7 (3) (1996) 793, https://doi.org/10.1109/tnn.1996.501738.

[23] D. Whitley, A Genetic Algorithm Tutorial, Statistics And, Computing 4 (2) (1994), https://doi.org/10.1007/bf00175354.

[24] J. Hennig, M. Elfner and J. Feder, Mph-Py/Mph: Mph 1.1.5, https://zenodo.org/record/6312347, 2022 (accessed 6 October 2022).

[25] N. Dohi, T. Takahashi, K. Minekawa, Y. Kawase, Power consumption and solid suspension performance of large-scale impellers in gas–liquid–solid three-phase stirred tank reactors, Chem. Eng. J. 97 (2004) 103–114, https://doi.org/10.1016/S1385-8947(03)00148-7.

[26] Thermoddem. https://thermoddem.brgm.fr/, 2021 (accessed: 22 April 2021).